Dynamic Equivalent Magnetic Network Analysis of an Axial PM Bearingless Flywheel Machine

ZHIYING ZHU [1,2], **(Member, IEEE), HAILANG ZHU**[1], **XINYA LI**[1], **JIN ZHU**[1],
AND MING CHENG[2], **(Fellow, IEEE)**
[1]School of Electric Power Engineering, Nanjing Institute of Technology, Nanjing 211167, China
[2]School of Electrical Engineering, Southeast University, Nanjing 210096, China

Corresponding author: Zhiying Zhu (zyzhu@njit.edu.cn)

ABSTRACT A nonlinear dynamic equivalent magnetic network model for an axial permanent magnet bearingless flywheel machine (APM-BFM) is proposed in this paper. The model focuses on analyzing the magnetic field changes at the air gap of the machine. According to the relative position of the stator and rotor, the magnetic circuit between the rotor and the suspension pole (the torque pole) is divided into 7 stages (8 stages), and dynamic equivalent magnetic network models are established. The local saturation coefficient is introduced to characterize the local magnetic saturation phenomenon of the rotor yoke during the rotation of the rotor. Using the proposed model and based on the obtained winding flux, the opposing electromotive forces and inductances of the suspension and torque windings of the APM-BFM are all analyzed and calculated. Finally, the validity of the proposed model is verified by finite element analysis (FEA).

INDEX TERMS Bearingless flywheel machine, equivalent magnetic network, local saturation coefficient, finite element analysis.

I. INTRODUCTION

Energy storage systems (ESSs) have a very important position in today's world; for instance, the next generation of smart grids without ESSs is analogous to a mobile phone without a battery [1]. Some kinds of ESSs are used in electrical systems, such as pumped hydro storage (PHS), battery energy storage (BES), supercapacitor energy storage (SES), superconducting magnetic energy storage (SMES), thermal energy storage (TES), and flywheel energy storage system (FESS) technologies. A FESS stores the motive energy in a high-speed rotating turntable connected to the machine shaft and releases the energy in the system when necessary [2], [3]. Hence, a FESS is a mechanical energy storage system. Compared with other ESSs, FESSs have several advantages, including high energy efficiency, fast response speed, strong instantaneous power, low maintenance, long life, and environmentally friendly features [4], [5]. However, a high-speed

flywheel can cause a machine to generate excessive heat, and the cooling device needed to ensure stable operation is costly. A magnetic bearing (MB) can realize a noncontact rotation of the shaft, which can reduce both heat and cost [6]. However, MBs also have disadvantages, including complex structures, limited critical speeds, and high maintenance costs. Hence, by combining an MB and a switched reluctance machine (SRM), a bearingless switched reluctance machine (BSRM), featuring a compact structure, high critical speed, and no friction, is an attractive solution [7]. This can be introduced into a FESS to form a bearingless flywheel machine (BFM). Nevertheless, a traditional BFM is a multivariable, highly nonlinear and strongly coupled system that can present a great challenges in high-performance control [8]–[10].

An axial PM bearingless flywheel machine (APM-BFM) uses a magnetic isolator to decouple the torque magnetic circuit and the suspension magnetic circuit from each other. The strong coupling between suspension force and torque in traditional BSRMs is resolved structurally [11]. It has inherently high speed, large torque, and high power density

The associate editor coordinating the review of this manuscript and approving it for publication was Qinfen Lu.

characteristics, which has attracted more attention in flywheel energy storage applications. However, the magnetic flux path of the APM-BFM presents a three-dimensional distribution in space, which greatly increases the difficulty of design and modeling [12]. Finite element analysis (FEA) is widely used by most scholars because of its high accuracy in the analysis of mechanical electromagnetic characteristics [13]. However, the structural parameters often need to be changed in the early stage of design. Although FEA results are accurate, the long calculation time precludes its application in initial electrical machine design. Reference [14] proposed that modeling the magnetic circuit with scalar magnetic potential can effectively shorten the calculation time of FEA, but the three-dimensional analysis method still takes considerable time. The magnetic circuit (MC) method has the advantages of a simple model and short solving time. The obtained solution results have great reference value in the early stage of design. Therefore, the MC method is a good solution for investigating the three-dimensional magnetic field of an APM-BFM [15]–[17]. However, the accuracy of the MC method cannot be guaranteed when considering the nonlinear magnetic permeability of the materials in the magnetic circuit.

The equivalent magnetic network (EMN) method combines FEA with the MC method, which can quickly and accurately calculate the electromagnetic characteristics of a machine [18]. The method divides the magnetic circuit into regular-shaped flux tubes according to the magnetic density distribution of the machine, and the number of flux tubes is much smaller than the number of mesh divisions in the FEA, which improves the solving speed of the model. Since the appropriate magnetic flux tube is selected according to the magnetic flux density, it can be considered that the magnetic density of each magnetic flux tube is the same, and the nonlinear problem of the magnetic material can be easily considered. The permeance is calculated according to the shape of the magnetic flux tube, and the magnetic flux path is determined strictly according to the magnetic flux distribution and geometric boundary determined in [19]–[22]. To reduce the model complexity, the leakage flux is usually ignored, and rough analysis is performed through a conventional EMN model instead of complicated mathematical calculations. Reference [23] proposed a method of combining MC and meshing. The method divides the reluctance part of the air gap into a fine reluctance grid, which improves the accuracy of the model. The magnetic permeability at the operating point of the stator and rotor core is obtained by interpolation, and the magnetic saturation of the stator and rotor is considered. However, multiple iterations are required, which greatly increases the amount of calculation. In [24], an EMN model of an axial PM machine was proposed, which can calculate the loss generated during the operation of the machine; the machine is divided into several parts for modeling separately, but the overall magnetic network topology is not given. Reference [25] proposed an EMN model of an induction machine. The local magnetic saturation

phenomenon is considered, and model has good accuracy. As the above-mentioned EMN models become more complex, the modeling accuracy and flexibility also change. In addition, the above EMN models are not suitable for an APM-BFM due to differences in structure.

This paper proposes a dynamic EMN model for an APM-BFM during the full rotation of the rotor. An appropriate flux tube is selected to be equivalent to the air gap flux in different shapes. EMN models of the APM-BFM torque magnetic circuit and the suspension magnetic circuit are established in different stages, and an overall dynamic EMN model of the APM-BFM is formed and given. Specifically, a local saturation coefficient is introduced to characterize the local saturation phenomenon. Finally, the results of FEA and the proposed dynamic EMN model are compared, and the results verify the validity of the model. Section II briefly introduces the structure and operating principle of the APM-BFM, while section III details the modeling process of the EMN. Section IV provides the EMN solution method, and section V concludes the paper.
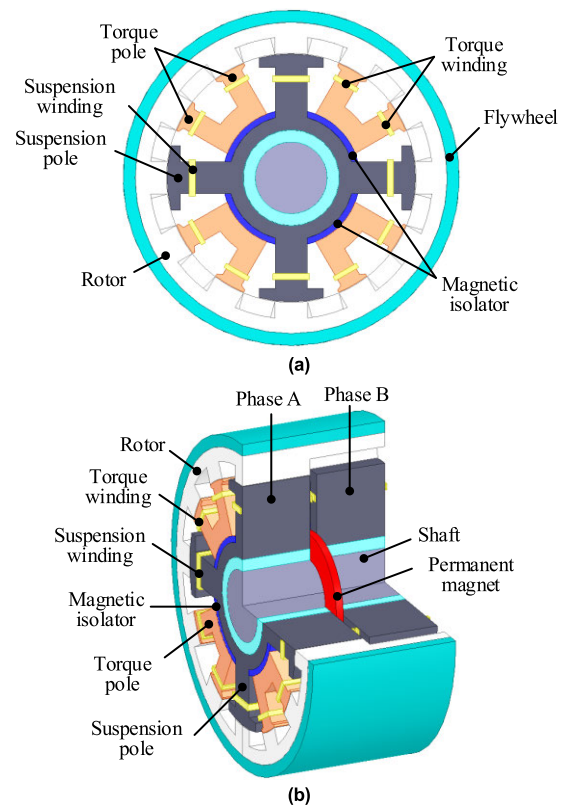

FIGURE 1. The structure of APM-BFM (a) Front view. (b) Side view.

II. STRUCTURE OF APM-BFM

Fig. 1 shows the structure of the APM-BFM. It includes two parts according to the number of phases (Phase A and Phase B) along the axial direction. Each phase is composed of a 12/12 pole structure of the inner stator and outer rotor. The 12 poles of the inner stator are composed of four suspension poles (wide tooth) and eight torque poles (narrow tooth).

Furthermore, the pole width of the torque pole is equal to the rotor pole width, which increases the electromagnetic torque and reduces the torque ripple. The pole width of the suspension pole is equal to a rotor pole pitch, which weakens the influence of the position angle change on the suspension force. In addition, an axially magnetized PM is installed in the middle. The intention can be summarized as it generates the bias magnetic flux that reduces the power consumption of the suspension winding. In addition, the flywheel and the machine are integrated together by the outer rotor structure. The special structure has several advantages, including improving axial utilization, reducing the size of the FESS, and improving the strength of the flywheel rotor and the instantaneous power of the machine. Specifically, magnetic isolators are installed between the suspension pole and the torque pole to realize the decoupling of the suspension force and the torque. In addition, the magnetic circuit between each rotor tooth and the suspension pole are the same during the entire rotation. Only the magnetic circuit between a single suspension pole and a single rotor tooth needs to be studied when establishing the EMN model. In the proposed FESS, the four degrees-of-freedom displacements of the rotor are measured by eight eddy current sensors installed at two ends of the stator shaft, as shown in Fig. 2(a) and (b). Furthermore, two auxiliary bearings are used to offer auxiliary support under special circumstances. The air gap of the auxiliary bearing is 0.2 mm to ensure safe operation and shutdown.

The radial path of the suspension magnetic flux is the path of the flux linkage Ψ_{sa} in Fig. 3(a). The axial path of the bias flux generated by the PM is the path of the flux linkage Ψ_{PM} in Fig. 3(b). The bias flux starts from the N pole, passes through the phase A suspension pole and the air gap, enters the outer rotor tooth, flows through the rotor yoke, passes through the air gap from the phase B rotor tooth, passes through the phase B suspension pole and the yoke, and enters the PM S pole to form the closed loop. Hence, the permeance in the magnetic circuit should include the presence of the air gap, yoke, tooth, and PM. The main parameters of the APM-BFM are listed in Table 1.

III. DYNAMIC EQUIVALENT MAGNETIC NETWORK
A. AIR GAP PERMEANCE OF SUSPENSION POLE
Two typical positions during the rotation of the rotor are listed in Fig. 4. Fig. 4(a) shows the alignment position of the rotor and the suspension pole, and the rotor tooth centerline coincides with the suspension pole centerline. In addition, the pole arc of the part where the stator and rotor teeth are aligned is 15°. The adjacent rotor teeth and torque poles also have aligned parts, as shown in Fig. 4(b), and the sum of the pole arcs of the aligned parts is 15°. Similarly, it can be seen that the aligned pole arcs are all 15° in the rotor rotation period. Then, the permeance of the aligned part remains unchanged during the rotor rotation period. Compared with the rest of the magnetic circuit between the torque poles and the rotor teeth, the magnetic circuit path of the alignment part is the shortest,
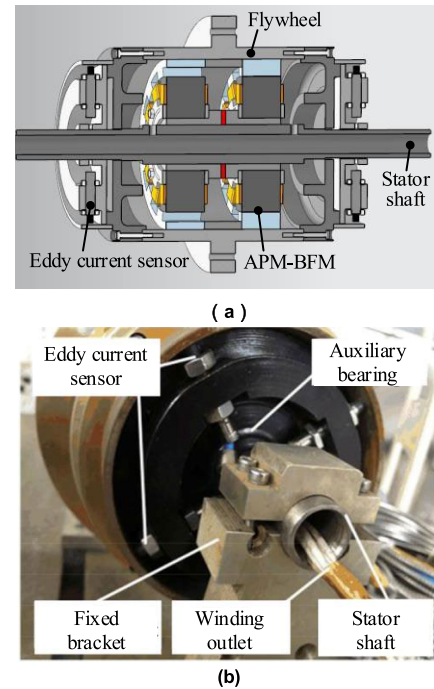

FIGURE 2. The specific FESS. (a) Structure. (b) Prototype.
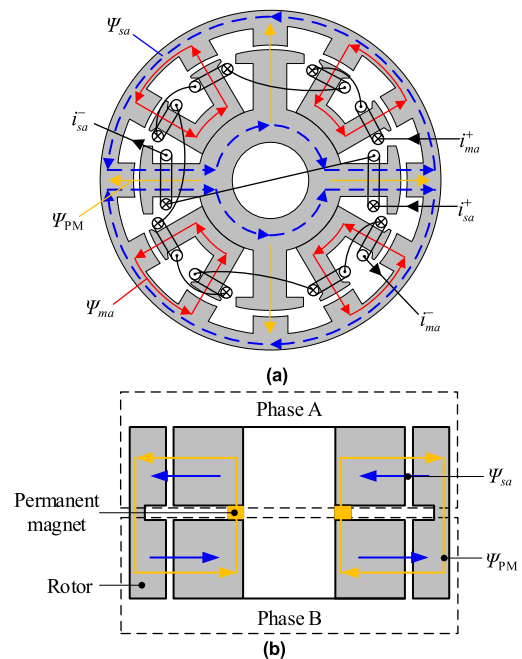

FIGURE 3. The magnetic circuit of the APM-BFM. (a) Radial magnetic circuit diagram (Phase A). (b) Axial magnetic circuit diagram.

resulting in the maximum permeance of the alignment part. The permeance has a great influence on the suspension force of the APM-BFM, and its constant value ensures the stability of the APM-BFM suspension output.

To study the suspension characteristics of the APM-BFM more accurately, it is necessary to conduct a more detailed analysis of the magnetic circuit between the torque poles and rotor teeth. The equivalent magnetic circuit of the partial

TABLE 1. Specifications of APM-BFM.

| Parameter	Value	Parameter	Value
rotor outer diameter [mm]	130	PM axial length [mm]	3
rotor inner diameter [mm]	102	PM outer diameter [mm]	50
rotor yoke height [mm]	7	PM inner diameter [mm]	30
suspension core inner diameter [mm]	30	suspension pole yoke thickness [mm]	10
torque core inner diameter [mm]	56	suspension pole arc [°]	30
torque pole yoke thickness [mm]	8	torque pole arc [°]	15
magnetic isolator thickness [mm]	3	rotor pole arc [°]	15
average air gap length [mm]	0.3	suspension winding turns	100
stack length [mm]	60	torque winding turns	80
core material	DW3 60_50	stator outer diameter [mm]	101.4
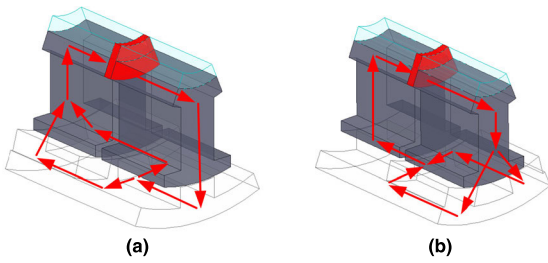
FIGURE 4. Typical position during rotor rotation. (a) Alignment. (b) Local alignment.
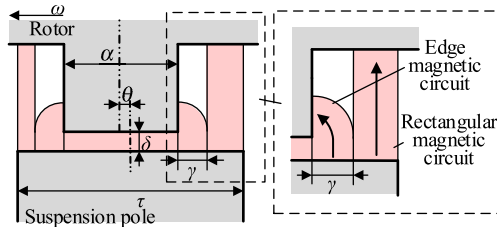

FIGURE 5. The relative position of suspension pole and rotor teeth.

magnetic circuit between the suspension pole and the torque pole is listed in Fig. 5. In Fig. 5, τ is the suspension pole arc, and α is the rotor pole arc. θ is the rotation angle of the rotor, $\theta = \omega t$, ω is the angular velocity of the rotor, δ is the air gap length, and γ is the maximum value of the pole arc in the edge magnetic circuit. The initial position angle $\theta = 0°$ is defined as the position where the suspension pole axis and the rotor pole axis coincide. In addition, the positive direction of the rotor rotation is counterclockwise.

According to the "minimum reluctance principle" of the magnetic circuit, γ satisfies formula (1).

$$\delta + \frac{1}{2}\pi(\gamma \cdot R_{sout}) = R_{rin} - R_{sout} \qquad (1)$$

where R_{sout} is the outer diameter of the torque pole and R_{rin} is the inner diameter of the rotor yoke. According to formula (1), the maximum value γ of the pole arc in the edge magnetic
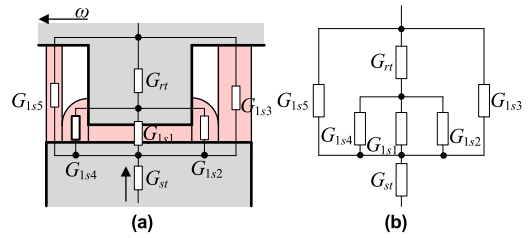

FIGURE 6. Stage 1. (a) Flux path. (b) Equivalent magnetic circuit.

circuit can be obtained. Then, the maximum value of the pole arc in the rectangular magnetic circuit is $15° - 2\gamma$.

The rotor rotation period is divided into 7 stages to analyze the air gap permeance. G_{rt} is the permeance of a single rotor tooth, and G_{st} is the permeance of the suspension pole core.

The rotor rotates from the initial position $\theta = 0°$ to $7.5°$-γ in stage 1, and the air gap equivalent magnetic circuit is shown in Fig. 6. The rotor rotates from the initial position until the rectangular magnetic circuit G_{1s5} gradually disappears.

As shown in Fig. 6(b), the total magnetic permeance at the suspension pole of stage 1 is expressed as:

$$G_{ats1} = \frac{(G_{1s} + G_{1s3} + G_{1s5}) \cdot G_{st}}{G_{1s} + G_{1s3} + G_{1s5} + G_{st}} \qquad (2)$$

where G_{1s} is the total permeance between the suspension pole and the current rotor tooth; $G_{1s} = \frac{(G_{1s1} + G_{1s2} + G_{1s4}) \cdot G_{rt}}{G_{1s1} + G_{1s2} + G_{1s4} + G_{rt}}$. G_{1s3} and G_{1s5} are the permeances of rectangular magnetic circuits between the suspension pole and the rotor yoke.

The range of the rotor rotation angle in stage 2 is $(7.5° - \gamma, 7.5°)$. The permeance G_{2s5} of the edge magnetic circuit gradually decreases. As θ increases, the distance between the suspension pole and the next rotor tooth continues to shrink. Then, the magnetic flux of the suspension pole starts to flow into the next rotor tooth, and the magnetic flux flow path is equivalent to a rectangular path with a 1/4 ring. The equivalent magnetic circuit is given in Fig. 7. In addition, the magnetic path of permeance G_{2s6} is irregular, and its value is very small compared with that of the magnetic circuit of the alignment part. To describe its change rule, take $G_{2s6} = G_{2s4}$.

As shown in Fig. 7(b), the total magnetic permeance at the suspension pole of stage 2 is expressed as:

$$G_{ats2} = \frac{(G_{2s} + G_{2s3} + G'_{2s}) \cdot G_{st}}{G_{2s} + G_{2s3} + G'_{2s} + G_{st}} \qquad (3)$$

where G_{2s} is the total permeance of the magnetic circuit between the suspension pole and the current rotor teeth; $G_{2s} = \frac{(G_{2s1} + G_{2s2} + G_{2s5}) \cdot G_{rt}}{G_{2s1} + G_{2s2} + G_{2s5} + G_{rt}}$. G'_{2s} is the total permeance of the magnetic circuit between the suspension pole and the next rotor teeth; $G'_{2s} = \frac{(G_{2s4} + G_{2s6}) \cdot G_{rt}}{G_{2s4} + G_{2s6} + G_{rt}}$. G_{2s3} is the permeance of the rectangular magnetic circuit between the suspension pole and the rotor yoke.

The rotor rotates from $\theta = 7.5°$ to $\theta = 7.5° + \gamma$ in stage 3. An alignment part appears between the suspension pole and the teeth of the next rotor, and the permeance G_{3s7} of the edge magnetic circuit gradually increases. The pole arc of the
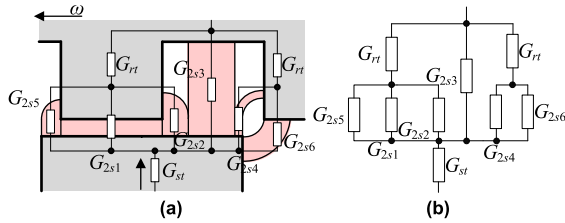
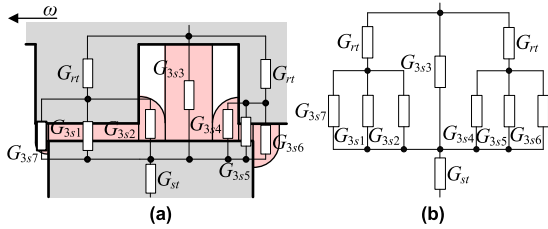**FIGURE 7.** Stage 2. (a) Flux path. (b) Equivalent magnetic circuit.

FIGURE 8. Stage 3. (a) Flux path. (b) Equivalent magnetic circuit.
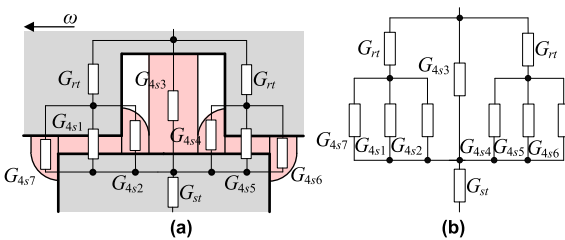

FIGURE 9. Stage 4. (a) Flux path. (b) Equivalent magnetic circuit.

aligned part between the adjacent rotor teeth and the suspension pole is always 15°, and the permeance of the remaining parts remains unchanged. Hence, the total permeance G_{ats3} at the suspension pole in stage 3 increases as G_{3s7} increases. The equivalent magnetic circuit is shown in Fig. 8.

As shown in Fig. 8(b), the total magnetic permeance at the suspension pole of stage 3 is expressed as:

$$G_{ats3} = \frac{(G_{3s} + G_{3s3} + G'_{3s}) \cdot G_{st}}{G_{3s} + G_{3s3} + G'_{3s} + G_{st}} \quad (4)$$

where G_{3s} is the total permeance of the magnetic circuit between the suspension pole and the current rotor teeth; $G_{3s} = \frac{(G_{3s1} + G_{3s2} + G_{3s7}) \cdot G_{rt}}{G_{3s1} + G_{3s2} + G_{3s7} + G_{rt}}$. G'_{3s} is the total permeance of the magnetic circuit between the suspension pole and the next rotor tooth; $G'_{3s} = \frac{(G_{3s4} + G_{3s5} + G_{3s6}) \cdot G_{rt}}{G_{3s4} + G_{3s5} + G_{3s6} + G_{rt}}$. G_{3s3} is the permeance of the rectangular magnetic circuit between the suspension pole and the rotor yoke.

The range of the rotor rotation angle in stage 4 is $(7.5° + \gamma, 22.5° - \gamma)$. Fig. 9 illustrates the equivalent magnetic circuit. In stage 4, the magnetic circuit of the part where the suspension pole and rotor teeth are aligned changes, and the rest of the magnetic circuit remains unchanged. The pole arc of the aligned part between the adjacent rotor teeth and the suspension pole is always 15°. Hence, the total permeance of the magnetic circuit between the suspension pole and rotor teeth is constant. The magnetic circuit structure of stage 4 is similar to that of stage 3, and the total permeance G_{ats4} is also consistent; hence, a detailed analysis is omitted.

The rotor rotates from $\theta = 22.5° - \gamma$ to $\theta = 22.5°$ in stage 5. The equivalent magnetic circuit is shown in Fig. 10.
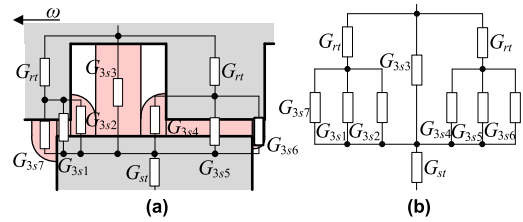

FIGURE 10. Stage 5. (a) Flux path. (b) Equivalent magnetic circuit.

In Fig. 10, as θ increases, the permeance G_{3s6} of the edge magnetic circuit decreases continuously, and the permeances of the remaining magnetic circuits remain unchanged. Hence, the total air gap permeance at the suspension pole is continuously reduced. The analysis results show that this stage is similar to stage 3. The air gap magnetic circuit between the suspension pole and the current rotor teeth is interchanged with the air gap magnetic circuit between the suspension pole and the next rotor teeth, and the changing trend of the total air gap permeance is opposite. In conclusion, stage 5 and stage 3 are symmetrical about stage 4. It can be further determined that stage 6 and stage 7 are symmetrical to stage 2 and stage 1 with respect to stage 4, respectively.

B. AIR GAP PERMEANCE OF TORQUE POLE

According to the "minimum reluctance principle", the critical angle of the magnetic circuit between the torque pole and rotor teeth is also γ. That is, the critical angle is the same as the suspension pole. The definition θ is also the same as the suspension pole. A cycle of the rotor rotation process is decomposed into 8 stages to realize the high-precision modeling of the APM-BFM. Then, the equivalent magnetic circuit at each stage is established. G_{rt} is the permeance of a single rotor tooth, and G_{str} is the permeance of the torque pole core.

Stage 1 is the alignment of the stator teeth and the rotor teeth, as shown in Fig. 11.

The total permeance G_{atr1} at the torque pole at this stage is:

$$G_{atr1} = \frac{G_{rt} G_{str} G_{1r1}}{G_{1r1} G_{str} + G_{rt} G_{str} + G_{rt} G_{1r1}} \quad (5)$$

where G_{1r1} is the air gap permeance. Since the torque pole is aligned with the rotor at this stage, there is no edge magnetic circuit. Hence, the torque of APM-BFM is zero at this time.

The range of the rotor rotation angle θ in stage 2 is $(0, \gamma)$. A fringe magnetic circuit appears between the torque pole and the rotor at this stage. The equivalent magnetic circuit is given in Fig. 12.

According to the basic knowledge of the circuit, the total permeance at the torque pole can be expressed as:

$$G_{atr2} = \frac{G_{rt} G_{str} G_{2r}}{G_{2r} G_{str} + G_{rt} G_{str} + G_{rt} G_{2r}} \quad (6)$$
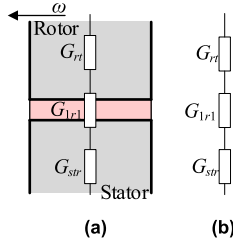
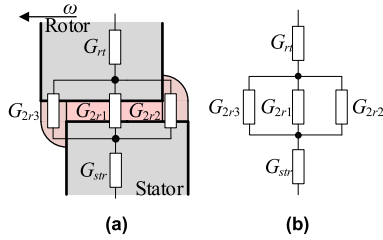**FIGURE 11.** Stage 1. (a) Flux path. (b) Equivalent magnetic circuit.

FIGURE 12. Stage 2. (a) Flux path. (b) Equivalent magnetic circuit.
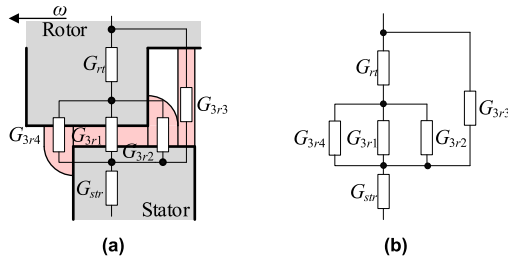

FIGURE 13. Stage 3. (a) Flux path. (b) Equivalent magnetic circuit.

where $G_{2r} = G_{2r1} + G_{2r2} + G_{2r3}$; G_{2r} is the air gap permeance.

The rotor rotates from $\theta = \gamma$ to $\theta = 15° - \gamma$ in stage 3. A rectangular magnetic circuit begins to appear in the torque pole and rotor yoke. The equivalent magnetic circuit is given in Fig. 13.

The total air gap permeance of the torque pole and rotor teeth is:

$$G_{atr3} = \frac{(G_{3r} + G_{3r3}) \cdot G_{str}}{G_{3r} + G_{3r3} + G_{str}} \qquad (7)$$

where G_{3r} is the total permeance between the torque pole and rotor teeth; $G_{3r} = \frac{(G_{3r1}+G_{3r2}+G_{3r4})\cdot G_{rt}}{G_{3r1}+G_{3r2}+G_{3r4}+G_{rt}}$. G_{3r3} is the total permeance between the torque pole teeth and the rotor yoke.

The rotor rotates from $\theta = 15° - \gamma$ to $\theta = 15°$ in stage 4. The flux path begins to appear between the torque pole and the next rotor tooth. The equivalent magnetic circuit is given in Fig. 14.

The total permeance at the torque pole in stage 4 is:

$$G_{atr4} = \frac{(G_{4r} + G_{4r3} + G'_{4r}) \cdot G_{str}}{G_{4r} + G_{4r3} + G'_{4r} + G_{str}} \qquad (8)$$

where G_{4r} is the total permeance of the magnetic circuit between the torque pole and the current rotor teeth; $G_{4r} = \frac{(G_{4r1}+G_{4r2}+G_{4r6})\cdot G_{rt}}{G_{4r1}+G_{4r2}+G_{4r6}+G_{rt}}$. G'_{4r} is the total permeance of the magnetic circuit between the torque pole and the next rotor teeth;
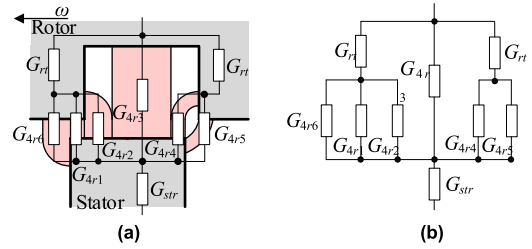

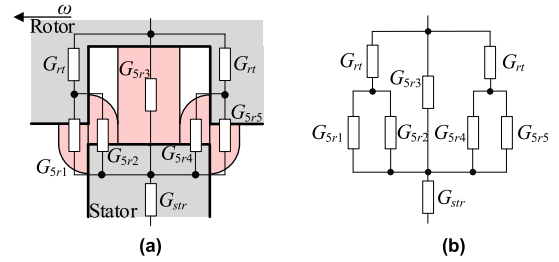**FIGURE 14.** Stage 4. (a) Flux path. (b) Equivalent magnetic circuit.

FIGURE 15. Stage 5. (a) Flux path. (b) Equivalent magnetic circuit.

$G'_{4r} = \frac{(G_{4r4}+G_{4r5})\cdot G_{rt}}{G_{4r4}+G_{4r5}+G_{rt}}$. G_{4r3} is the permeance of the magnetic circuit from the torque pole to the rotor yoke.

The rotor rotation angle $\theta = 15°$ is defined as stage 5. The equivalent magnetic circuit is shown in Fig. 15.

The total permeance at the torque pole in stage 5 from Fig. 15(b) is:

$$G_{atr5} = \frac{(G_{5r} + G_{5r3} + G'_{5r}) \cdot G_{str}}{G_{5r} + G_{5r3} + G'_{5r} + G_{str}} \qquad (9)$$

where G_{5r} is the total permeance of the magnetic circuit between the torque pole and the current rotor teeth; $G_{5r} = \frac{(G_{5r1}+G_{5r2})\cdot G_{rt}}{G_{5r1}+G_{5r2}+G_{rt}}$. G'_{5r} is the total permeance of the magnetic circuit between the torque pole and the next rotor teeth; $G'_{5r} = \frac{(G_{5r4}+G_{5r5})\cdot G_{rt}}{G_{5r4}+G_{5r5}+G_{rt}}$. G_{5r3} is the permeance of the magnetic circuit from the torque pole to the rotor yoke. The magnetic circuit between the torque pole and the current rotor tooth is the same as the magnetic circuit between the torque pole and the next rotor tooth. Then, the torque that causes the rotor to rotate counterclockwise and clockwise is the same. Hence, the torque of APM-BFM in stage 5 is zero.

The result of analyzing the rotor rotation law shows that stage 6 is similar to stage 4. That is, the magnetic circuit between the torque pole and the next rotor tooth (the current rotor tooth) in stage 6 is the same as the magnetic circuit between the torque pole and the current rotor tooth (the next rotor tooth) in stage 4. In addition, stage 7 and stage 8 are similar to stage 3 and stage 2, respectively. Only the magnetic circuit between the torque pole and the current rotor tooth is interchanged with the magnetic circuit between the torque pole and the next rotor tooth. After stage 8, the rotor returns to the initial position $\theta = 0°$, and the rotor completes one cycle of rotation. In conclusion, the electromagnetic characteristics of the APM-BFM torque during one rotation of the rotor are symmetrical about stage 5.

C. ANALYSIS OF EQUIVALENT MAGNETIC FLUX TUBE

Depending on the shape of the magnetic circuit, the air gap magnetic circuit can be equivalent to three types of flux tubes. The magnetic flux tubes are the rectangular magnetic flux tube in Fig. 16(a), the rectangular magnetic flux tube with a 1/4 circle in Fig. 16(b), and the rectangular magnetic flux tube with a 1/4 ring in Fig. 16(c). The actual tooth shape of the machine is an arc. It is equivalent to a straight line in the model, and the straight line has little effect on the accuracy of the model. Hence, the permeance can be calculated as a straight line. The calculation formula is given in formulas (10)-(12).

According to the basic calculation formula of permeance, the permeance of a rectangular magnetic flux tube is

$$G_1 = \frac{u_0 h X_1}{\delta} \tag{10}$$

The permeance of a rectangular magnetic flux tube with a 1/4 circle is

$$G_2 = \frac{2u_0 h}{\pi} \ln[1 + \frac{\pi X_1}{2\delta}] \tag{11}$$

The permeance of a rectangular magnetic flux tube with a 1/4 ring is

$$G_3 = \frac{2u_0 h}{\pi} \ln[1 + \frac{\pi X_1}{\pi C_1 + 2\delta}] \tag{12}$$

where u_0 is the vacuum permeability, h is the tooth height of the suspension teeth, X_1 is the width of the flux tube, and C_1 is the inner diameter of the rectangular magnetic flux tube with a 1/4 ring.

Since the core permeance is much larger than the air gap permeance, the core permeance is not further divided. However, the verification results show that the rotor core has local magnetic saturation.

In Fig. 17, the total permeance of the suspension magnetic circuit begins to increase when the rotor rotates to stage 3. Then, the magnetic flux flowing in the rotor core increases, and local magnetic saturation occurs in the rotor yoke. The air gap permeance does not change in stage 4, and the rotor yoke is always in local magnetic saturation. The local saturation coefficient is introduced to reflect the saturation of the rotor core in stage 3 and is denoted as K_{st}. The expression is expressed as:

$$K_{st} = 1 - K(\theta - 7.5°) \tag{13}$$

where θ is the rotation angle of the rotor and K is the correction factor.

D. EMN MODEL OF APM-BFM

Fig. 18 below shows the EMN of the APM-BFM. The half model of the A-phase radial magnetic circuit is given in Fig. 18(a) due to the model symmetry. Phase A and phase B have the same structure in the APM-BFM, and only the rotor pole axis differs by 15°. Then, the radial equivalent magnetic circuit of phase B is the same as that of phase A.
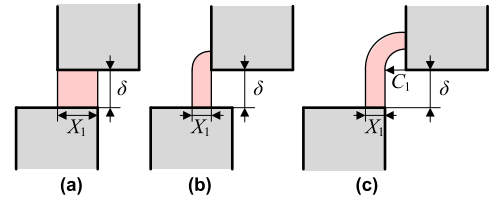

FIGURE 16. Atypical flux tube. (a) Rectangle. (b) Rectangle with 1/4 circle. (c) Rectangular with 1/4 ring.
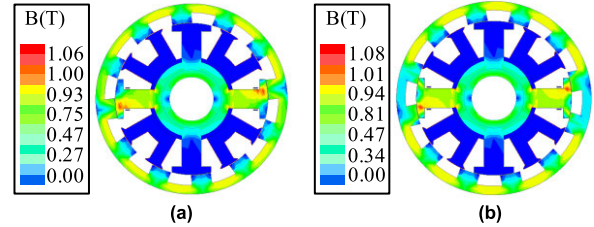

FIGURE 17. Saturation depth of rotor yoke. (a) Rotor rotates to 7.5°. (b) Rotor rotates to 12°.

The large cross-sectional area of the suspension pole yoke makes it difficult to saturate. Its permeance is much larger than the air gap permeance, and ignoring this part of the permeance has little effect on the calculation accuracy of the EMN model. G_{atsx} is the total permeance of the magnetic circuit between the suspension pole and rotor teeth at each stage. G_{st} is the permeance of the suspension pole core, F_{sa} is the magnetomotive force of the suspension winding, and G_{ry1} is the permeance of the rotor yoke. The calculation formulas are as follows:

$$G_{st} = \frac{u_0 u_s h w_s}{l_s} \tag{14}$$

$$F_{sa} = N_{sa} i_{sa} \tag{15}$$

$$G_{ry1} = \frac{u_0 u_r h l_e}{6\pi(R_{rout} + R_{rin})} \tag{16}$$

where u_s is the relative permeability of the suspension pole core and w_s and l_s are the tooth width and tooth length of the suspension pole, respectively. N_{sa} and i_{sa} are the turns and current of the suspension winding, respectively. u_r and l_e are the relative permeability and the thickness of the rotor yoke, respectively. R_{rout} and R_{rin} are the outer and inner diameters of the rotor yoke, respectively.

G_{atrx} is the total permeance of the magnetic circuit between the stator and rotor teeth at each stage of torque in Fig. 18(a). G_{str} is the core permeance of the torque pole. In addition, F_{ma} is the magnetomotive force of the torque winding. The calculation formulas are as follows:

$$G_{str} = \frac{u_0 u_t h w_r}{l_r} \tag{17}$$

$$F_{ma} = N_{ma} i_{ma} \tag{18}$$

where u_t is the relative permeability of the torque core and w_r and l_r are the width and length of the torque pole, respectively. N_{ma} and i_{ma} are the turns and current of the torque winding, respectively.
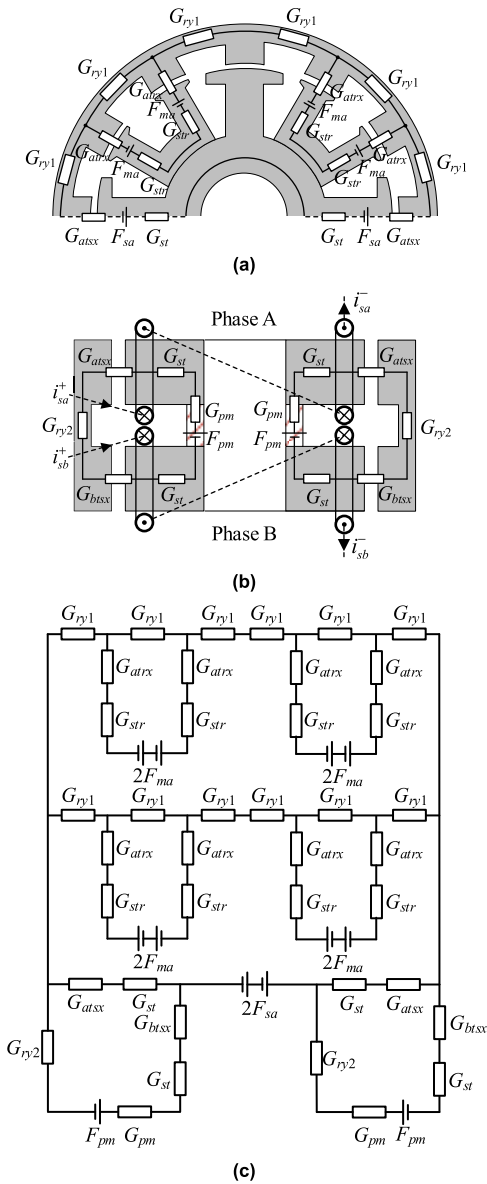
FIGURE 18. EMN model of APM-BFM. (a) Radial equivalent magnetic circuit. (b) Axial equivalent magnetic circuit. (c) A-phase EMN.

Fig. 18(b) shows the axial equivalent magnetic circuit of the APM-BFM. Since the permeance of the rotor yoke is much larger than the air gap permeance, it is equivalent to a permeance G_{ry2}, which has little effect on the accuracy of the model. G_{atsx} and G_{btsx} are the total air gap permeance of the suspension magnetic circuit in each stage of phase A and phase B, respectively. G_{pm} and F_{pm} are the permeance and the magnetomotive force of the PM, respectively. The calculation formulas are as follows:

$$G_{ry2} = \frac{u_0 u_r l_e w_r}{h} \qquad (19)$$

$$G_{pm} = \frac{u_0 u_{pm} \pi \left(l_{pmo}^2 - l_{pmi}^2\right)}{h_{pm}} \qquad (20)$$

$$F_{pm} = \frac{B_{rm} h_{pm}}{u_0 u_{pm}} \qquad (21)$$

where u_{pm} is the relative permeability of the PM and l_{pmo} and l_{pmi} are the outer and inner diameters of the PM, respectively. B_{rm} and h_{pm} are the remanence and height of the PM, respectively.

The A-phase EMN model of the APM-BFM is given in Fig. 18(c). The structure of phase B is the same as that of phase A, except that the rotor pole axis differs by 15°. Hence, the EMN of phase B is similar to that of phase A.

IV. SOLUTION OF EMN

The A-phase EMN model in Fig. 18 is solved. Based on Equation (22), the flux linkage curve of the suspension winding and torque winding is obtained when $i_{sa} = 1.5$A and $i_{ma} = 0.85$A, as shown in Fig. 19.

$$\Psi = N \cdot F \cdot G_t \qquad (22)$$

where Ψ is the flux linkage of the winding, N is the number of winding turns, F is the magnetomotive force of the winding, and G_t is the total permeance of the magnetic circuit.
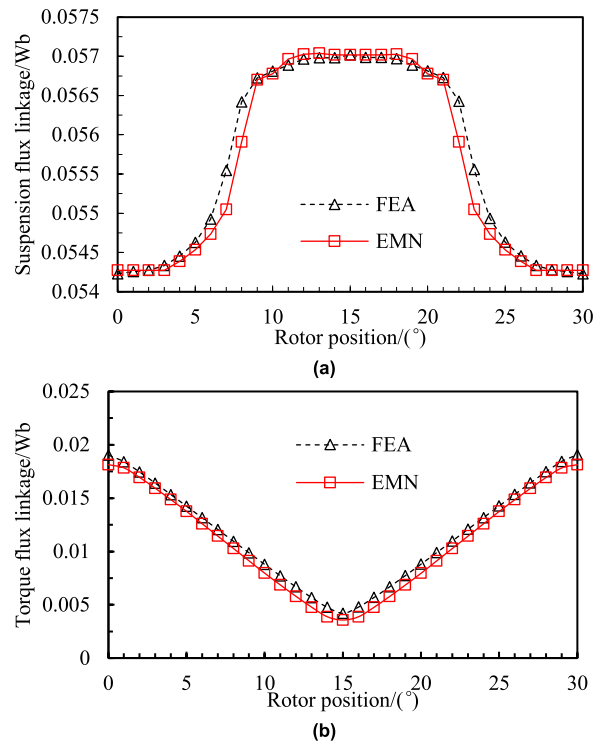
FIGURE 19. Comparison of flux linkage. (a) Suspension flux linkage. (b) Torque flux linkage.

The effect of curve fitting from 5° to 10° is not ideal in Fig. 19(a). This is because the magnetic flux does not strictly follow the rectangle with a 1/4 ring path when passing through the tooth tip, and its path is irregular. Here, to express the change in the air gap permeance, it is equivalent to a rectangle with a 1/4 ring path for calculation. Then, the result of the EMN model is consistent with the trend of

FIGURE 20. Comparison of opposing EMF. (a) Suspension opposing EMF. (b) Torque opposing EMF.
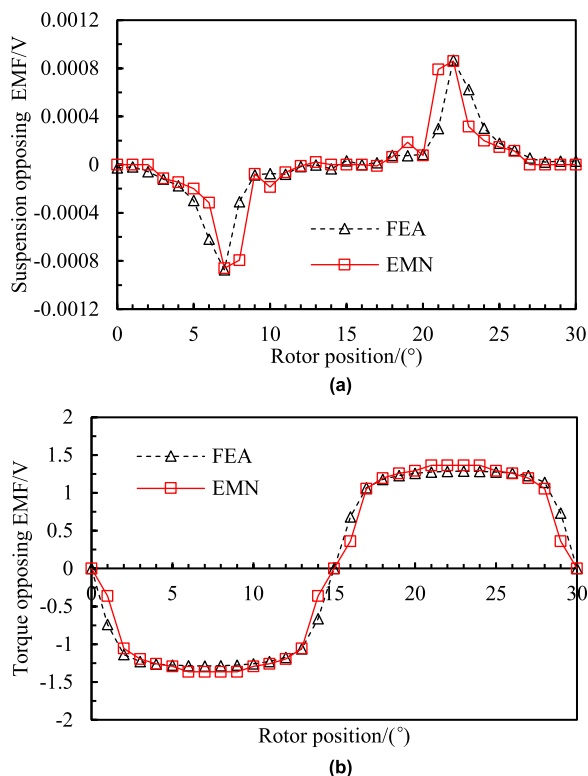

FIGURE 21. Comparison of inductance. (a) Suspension inductance. (b) Torque inductance.

FEA during the full period. In addition, the EMN model can effectively reflect the full-period torque flux linkage of the APM-BFM.

By using Equation (23), the opposing electromotive force (EMF) of the suspension winding and torque winding is obtained when $i_{sa} = 1.5$ A and $i_{ma} = 0.85$A, as shown in Fig. 20.

$$e = -\frac{d\Psi}{dt} \quad (23)$$

where e is the opposing EMF of the winding.

The opposing EMF curve of the suspension winding obtained by the EMN model fluctuates greatly at the peak in Fig. 20(a). It is due to the fact that the magnetic flux does not strictly follow the rectangle with a 1/4 ring path when passing through the tooth tip, and its path is irregular. Here, to express the change in the air gap permeance, it is equivalent to a rectangle with a 1/4 ring path for calculation. Then, the curve coincides with the results obtained by FEA, and the trend of opposing EMF is still clearly expressed. In Fig. 20(b), the opposing EMF curve of the torque winding obtained by the EMN model is negative at $0 \sim 15°$, positive at $15 \sim 30°$, and zero at $0°$, $15°$, and $30°$. This accords with the FEA result.

According to formula (24), the inductance of the suspension winding and torque winding is solved when $i_{sa} = 1.5$A and $i_{ma} = 0.85$A, as shown in Fig. 21.
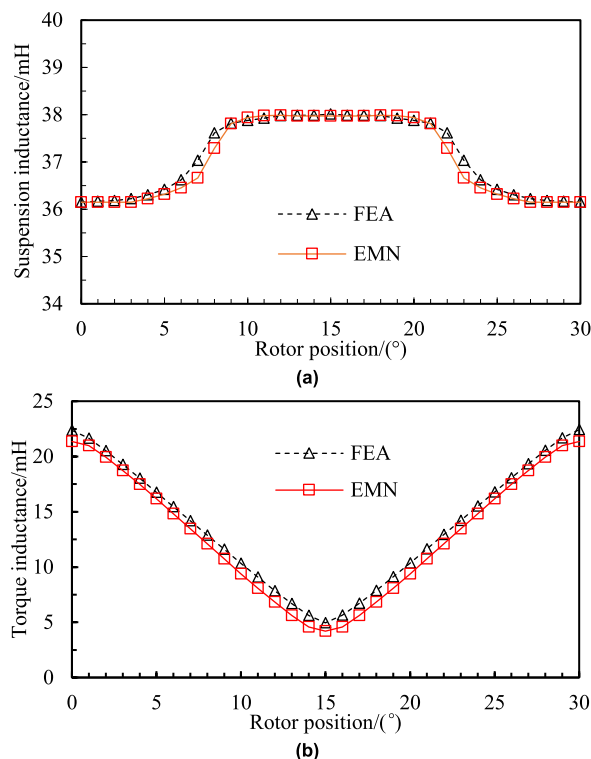
$$L = N^2 \cdot G_t \quad (24)$$

where L is the inductance of the winding.

In Fig. 21(a), the maximum peak-to-valley value of the suspension winding inductance during the whole cycle is 1.84 mH, which accounts for 4.97% of the average inductance. Hence, the inductance of the suspension winding fluctuates less during the full cycle. The torque winding inductance is the smallest when $\theta = 15°$ in Fig. 21(b). At this moment, the total permeance of the torque magnetic circuit is the smallest, which conforms to the structural design of the APM-BFM.

TABLE 2. Comparison of FEA and Proposed EMN methods.

Method	Comparison item	
	Number of grids	Time cost/min
FEA	16653	43.35
EMN	40	1.05

As shown below in Table 2, the time taken by FEA and the EMN model to obtain the results is given. The number of meshes subdivided in the FEA is 16653, and the simulation time is 43.35 minutes. However, the number of meshes of the EMN model is 40, and the calculation time is only 1.05 minutes. Therefore, compared with FEA, the proposed EMN model has a simple structure and high computational efficiency with high prediction accuracy.

V. CONCLUSION

This paper has established an EMN model for a new APM-BFM. The three-dimensional magnetic circuit of the APM-BFM is converted to a two-dimensional EMN model, which significantly simplifies the magnetic circuit solving process. The variations in the air-gap equivalent permeance at different rotor positions are considered and modeled. To characterize the local magnetic saturation phenomenon during the rotation of the rotor, a correcting coefficient of the rotor yoke permeance is introduced. The analysis results have confirmed the validity and accuracy of the proposed EMN model. In addition, the calculation time of the proposed model is much less than that of FEA. This can help to greatly improve the efficiency of machine design.

The APM-BFM studied in this paper has serious magnetic leakage due to its complex structure and complicated magnetic circuit. For electromagnetic performance prediction in the preliminary design of a machine, the proposed model is sufficient with fast computation and acceptable accuracy. However, to improve the model accuracy further, a more detailed network of the magnetic circuit, e.g., the magnetic flux leakage, should be considered and will be the topic of future research.

REFERENCES

[1] V. A. Boicea, "Energy storage technologies: The past and the present," *Proc. IEEE*, vol. 102, no. 11, pp. 1777–1794, Nov. 2014.

[2] Y. Zhang, W. Zhang, F. Gao, S. Gao, and D. J. Rogers, "A switched-capacitor interleaved bidirectional converter with wide voltage-gain range for super capacitors in EVs," *IEEE Trans. Power Electron.*, vol. 35, no. 2, pp. 1536–1547, Feb. 2020.

[3] Z. Weiyu, Y. Hengkun, and Z. Huangqiu, "Key technologies and technical bottleneck analysis of flywheel battery systems for electric vehicle," *Proc. CSEE*, vol. 38, no. 18, pp. 5568–5581, 2018.

[4] H. H. Abdeltawab and Y. A.-R.-I. Mohamed, "Robust energy management of a hybrid wind and flywheel energy storage system considering flywheel power losses minimization and grid-code constraints," *IEEE Trans. Ind. Electron.*, vol. 63, no. 7, pp. 4242–4254, Jul. 2016.

[5] S. M. Mousavi G, F. Faraji, A. Majazi, and K. Al-Haddad, "A comprehensive review of flywheel energy storage system technology," *Renew. Sustain. Energy Rev.*, vol. 67, pp. 477–490, Jan. 2017.

[6] A. M. Gee and R. W. Dunn, "Analysis of trackside flywheel energy storage in light rail systems," *IEEE Trans. Veh. Technol.*, vol. 64, no. 9, pp. 3858–3869, Sep. 2015.

[7] Z. Hao, Q. Yu, X. Cao, X. Deng, and X. Shen, "An improved direct torque control for a single-winding bearingless switched reluctance motor," *IEEE Trans. Energy Convers.*, vol. 35, no. 3, pp. 1381–1393, Sep. 2020.

[8] H. Wang, J. Bao, B. Xue, and J. Liu, "Control of suspending force in novel permanent-magnet-biased bearingless switched reluctance motor," *IEEE Trans. Ind. Electron.*, vol. 62, no. 7, pp. 4298–4306, Jul. 2015.

[9] Y. Huang, F. Huang, Y. Yuan, F. Yang, and K. Xie, "Design and analysis of a novel bearingless segmented switched reluctance motor," *IEEE Access*, vol. 7, pp. 94342–94349, 2019.

[10] X. Cao, J. Zhou, C. Liu, and Z. Deng, "Advanced control method for a single-winding bearingless switched reluctance motor to reduce torque ripple and radial displacement," *IEEE Trans. Energy Convers.*, vol. 32, no. 4, pp. 1533–1543, Dec. 2017.

[11] Z. Zhu, J. Wang, and M. Cheng, "A novel axial split phase bearingless flywheel machine with Hybrid-Inner-Stator permanent magnet-based structure," *IEEE Trans. Energy Convers.*, early access, Dec. 16, 2020, doi: 10.1109/TEC.2020.3045143.

[12] C. Yu, S. Niu, S. L. Ho, and W. N. Fu, "Magnetic circuit analysis for a magnetless double-rotor flux switching motor," *IEEE Trans. Magn.*, vol. 51, no. 11, pp. 1–5, Nov. 2015.

[13] K. Yamazaki and Y. Kanou, "Rotor loss analysis of interior permanent magnet motors using combination of 2-D and 3-D finite element method," *IEEE Trans. Magn.*, vol. 45, no. 3, pp. 1772–1775, Mar. 2009.

[14] Z. Wenpeng, S. Jinhao, and T. Guanzhen, "Scalar potential method in processing current-carrying regions for 3D field of transverse flux machine," *Trans. China Electrotech. Soc.*, vol. 21, no. 6, pp. 65–69, 88, 2006.

[15] X. Da, Z. Xuming, and L. Mingyao, "Electromagnetic performance analysis of axial field flux-switching permanent magnet machine using equivalent magnetic circuit method," *Electr. Mach. Control Appl.*, vol. 44, no. 11, pp. 79–84, 2017.

[16] K. J. W. Pluk, J. W. Jansen, and E. A. Lomonova, "3-D hybrid analytical modeling: 3-D Fourier modeling combined with mesh-based 3-D magnetic equivalent circuits," *IEEE Trans. Magn.*, vol. 51, no. 12, pp. 1–14, Dec. 2015.

[17] W. Di and G. Chenglin, "3D magnetic circuit analysis of a novel transverse flux permanent magnet machine," *Proc. CSEE*, vol. 33, no. 30, pp. 90–95, 2010.

[18] J.-H. Sim, D.-G. Ahn, D.-Y. Kim, and J.-P. Hong, "Three-dimensional equivalent magnetic circuit network method for precise and fast analysis of PM-assisted claw-pole synchronous motor," *IEEE Trans. Ind. Appl.*, vol. 54, no. 1, pp. 160–171, Jan. 2018.

[19] W. Lei, L. Guangyou, and Z. Qiang, "Network-varying equivalent magnetic circuit modeling of a flux-reversal machine," *Trans. China Electrotech. Soc.*, vol. 23, no. 8, pp. 18–23, 2008.

[20] Y. Le, J. Sun, and B. Han, "Modeling and design of 3-DOF magnetic bearing for high-speed motor including eddy-current effects and leakage effects," *IEEE Trans. Ind. Electron.*, vol. 63, no. 6, pp. 3656–3665, Jun. 2016.

[21] Z. Changjin and C. Zhihui, "Nonlinear dynamic equivalent magnetic network model analysis of transverse flux permanent magnet synchronous motor," *Proc. CSEE*, vol. 39, no. 1, pp. 307–314, 2019.

[22] J. Wang and J. Zhu, "A simple method for performance prediction of permanent magnet eddy current couplings using a new magnetic equivalent circuit model," *IEEE Trans. Ind. Electron.*, vol. 65, no. 3, pp. 2487–2495, Mar. 2018.

[23] G. Liu, S. Jiang, W. Zhao, and Q. Chen, "Modular reluctance network simulation of a linear permanent-magnet Vernier machine using new mesh generation methods," *IEEE Trans. Ind. Electron.*, vol. 64, no. 7, pp. 5323–5332, Jul. 2017.

[24] H. Yunkai and Z. Tao, "Efficiency optimization design of axial flux permanent magnet machines using magnetic equivalent circuit," *Trans. China Electrotech. Soc.*, vol. 30, no. 2, pp. 73–78, 2015.

[25] M. Amrhein and P. T. Krein, "Induction machine modeling approach based on 3-D magnetic equivalent circuit framework," *IEEE Trans. Energy Convers.*, vol. 25, no. 2, pp. 339–347, Jun. 2010.

ZHIYING ZHU (Member, IEEE) received the B.Sc., M.Sc., and Ph.D. degrees from the School of Electrical Engineering, Jiangsu University, Zhenjiang, China, in 2008, 2011, and 2013, respectively, all in electrical engineering.

Since 2013, he has been with the Nanjing Institute of Technology, where he is currently an Associate Professor with the School of Electric Power Engineering. He was a Postdoctoral Research Associate with Southeast University, Nanjing, China, from 2017 to 2018, and a Visiting Scholar with The University of Sheffield, Sheffield, U.K., from 2018 to 2019. His research interests include flywheel energy storage systems, bearingless electrical machines, renewable energy generation, and electric drives for electric and hybrid electric vehicles.

HAILANG ZHU was born in Anqing, Anhui, China, in 1996. He received the B.Sc. degree from the School of Electric Power Engineering, Nanjing Institute of Technology, Nanjing, China, in 2018, where he is currently pursuing the master's degree. His main research interest includes the design and application of bearingless machines.

JIN ZHU was born in Yangzhou, Jiangsu, China, in 1995. He received the B.Sc. degree from the School of Electric Power Engineering, Nanjing Institute of Technology, Nanjing, China, in 2018, where he is currently pursuing the master's degree. His main research interest includes characteristic analysis and the optimization design of bearingless machines.

MING CHENG (Fellow, IEEE) received the B.Sc. and M.Sc. degrees from the Department of Electrical Engineering, Southeast University, Nanjing, China, in 1982 and 1987, respectively, and the Ph.D. degree from the Department of Electrical and Electronic Engineering, The University of Hong Kong, Hong Kong, in 2001, all in electrical engineering.

Since 1987, he has been with Southeast University, where he is currently a Chair Professor with the School of Electrical Engineering and the Director of the Research Center for Wind Power Generation. From January 2011 to April 2011, he was a Visiting Professor with the Wisconsin Electric Machine and Power Electronics Consortium, University of Wisconsin, Madison, WI, USA. He has authored or coauthored more than 350 technical articles and four books and holds 100 patents in these areas. His teaching and research interests include electrical machines, motor drives for EV, and renewable energy generation.

Dr. Cheng is a Fellow of the Institution of Engineering and Technology. He has served as an organizing committee member and the chair for many international conferences. From 2015 to 2016, he was a Distinguished Lecturer of the IEEE Industry Application Society.

XINYA LI was born in Taizhou, Jiangsu, China, in 1999. She received the B.Eng. degree from the Jiangsu University of Technology, Changzhou, China, in 2020. She is currently pursuing the master's degree with the Nanjing Institute of Technology. Her main research interests include flywheel energy storage systems for electric power systems, renewable energy generation, and electric vehicles.

● ● ●